# TEM bright field imaging of thick specimens: nodes in Thon ring patterns

Willem Tichelaar[a,b,*], Wim J.H. Hagen[c], Tatiana E. Gorelik[b], Liang Xue[c,d], Julia Mahamid[c]

[a] *Corrected Electron Optical Systems GmbH, Englerstrasse 28, Heidelberg, 69126, Germany*
[b] *Central Facility of Electron Microscopy, Ulm University, Albert-Einstein-Allee 11, Ulm, 89081, Germany*
[c] *Structural and Computational Biology Unit, European Molecular Biology Laboratory, Meyerhofstrasse 1, Heidelberg, 69117, Germany*
[d] *Collaboration for joint PhD degree between EMBL and Heidelberg University, Faculty of Biosciences*

A B S T R A C T

The thickness of an object will, at some point, exceed the depth of field of a transmission electron microscope; the value at which this occurs, depends on the resolution and the wavelength considered. An image is then no longer a true projection of the 3D structure. This effect will be expressed in the power spectrum. Here, we first demonstrate this phenomenon experimentally, using carbon foils of different thicknesses and working at 40, 60, 80 and 300 kV. Since we determined the thicknesses of the foils by tomography, we are also able to confirm experimentally that in the case of a thick object, the Thon ring pattern can be described as the sum of the power spectra originating from thin, independently scattering slices. Thus, a sinc function envelope is observed that attenuates the Thon rings' amplitudes, yielding "nodes" in the pattern at which the amplitudes are zero. These nodes move to lower spatial frequencies with decreasing acceleration voltages and increasing thicknesses. Conversely, the object thickness can be directly derived from node positions at a particular acceleration voltage. We validate our approach by applying it to frozen-hydrated bacteria with experimentally determined thicknesses. Our model will contribute to more reliably determining the defocus to be used with contrast transfer function correction for thicker objects and at lower acceleration voltages.

## 1. Introduction

Three-dimensional (3D) image reconstruction is based on the assumption that an image is a 2D projection of the 3D structure. However, this assumption breaks down if the object does not obey the weak phase approximation or if its thickness exceeds the depth of field of the microscope. First describing the latter phenomenon in detail, DeRosier [1] found, that an object being too thick to be represented by a single amount of defocus can be regarded equivalent to it being too thick to consider the surface of the Ewald sphere as flat; the radius of the Ewald sphere is $1/\lambda$. In the latter approximation, pairs of beams intersecting the Ewald sphere at symmetric scattering angles about the incident beam are no longer related by $\mathbf{g}$ and $-\mathbf{g}$ reciprocal coordinates. Thus, the image is composed of Fourier coefficients not being Friedel pairs, *i.e.* not being complex conjugates of one another. In this case, special measures have to be taken to extract the Fourier components from the image.

Following the line of thought that the object is too thick to be represented by one single defocus, one could consider the specimen to consist of a series of infinitesimally thin, independently scattering slices, each with its own defocus. One could then sum the contrast transfer functions (CTFs) for these slices; the scattering factor can be taken out of the integral in the case of a homogeneous, amorphous object. Trying to understand the appearance of the power spectrum (or, diffractogram, as it used to be called), one would just have to square the result of the integration. Alternatively, one could integrate the power spectra of these slices. We will come back to the first approach in the Discussion. The second approach was followed by De Rosier [1] and by McMullan *et al.* [2].

From the integrals, these authors derived analytical expressions to describe the Thon ring patterns. Plots of these functions show that the intensities for the Thon rings, wavering around a value of 0.5, are increasingly damped with increasing spatial frequencies, though in an oscillating manner, leading to the appearance of what we name "nodes". McMullan *et al.* note that the observed sinc-function ringing that is observed "arises from the fixed thickness and uniform (top-hat) profile of the scattering". For cryo-specimens, they postulate that it may be more appropriate to add a "cosine profile" to the integral and to use the analytical expression thus derived. When using the respective functions for fits with the rotational average of a Thon ring pattern of amorphous ice, the authors could not discriminate between the two, mainly because the object thickness was unknown, but also because of

---

the noise in the power spectrum, limiting the clarity with which a node could be identified and precluding the detection of higher nodes.

In this work, we present results for objects of known thicknesses, in part obtained by using relatively high electron doses at relatively high resolution; also, different wavelengths (acceleration voltages) were applied. The experimental spectra allow a direct fit with results of numerical integrations of the square of the CTF over the object thickness. The merits of this kind of fitting will be discussed when it is compared to classical fitting of just the CTF in view of finding the defocus for appropriate CTF correction in the case of thick objects. We also put our results in the perspective of possibly applying acceleration voltages lower than 300 kV for imaging biological specimens, which has been advocated recently [3,4].

## 2. Materials and Methods

### 2.1. Specimen preparation

Amorphous carbon film was deposited onto mica via e-beam evaporation in a BALZERS BAF 400T machine (Balzers, Liechtenstein), using a quartz crystal for thickness monitoring. The foil thickness was assessed measuring the optical densities on the glass adjacent to where the mica sheet was lying during the evaporation (an optical density of 0.01 was assumed to correspond to a carbon film thickness of 1 nm [5]). Floated off onto a water surface, the carbon foil was fragmented, and small strips were layered onto 300 mesh grids in three successive steps, yielding specimens with at least three object thicknesses. For tomography, gold was deposited onto both sides of the carbon specimen, as 5 or 10 nm protein A-conjugated gold beads (Department of Cell Biology, University Medical Center Utrecht, The Netherlands), or as grains via e-beam evaporation in the BALZERS BAF 400T machine.

Wild-type *Mycoplasma pneumoniae* M129 (ATTC 29342) were cultivated in cell culture flasks with modified Hayflick medium (14.7 g/L Difco™ PPLO (Becton Dickinson, U.S.A.), 20% (v/v) Gibco™ horse serum (New Zealand origin, Life Technologies, Carlsbad, U.S.A), 100 mM Hepes-Na (pH 7.4), 1% (w/w) glucose, 0.002% (w/w) phenol red and 1,000 U/mL penicillin G). For cryo-EM grid preparation, 200-mesh gold grids with Quantifoil holey support (R2/1, Quantifoil Micro Tools, Jena, Germany) were glow discharged for 45 sec and then sterilized under UV irradiation. After inoculation, *M. pneumonia* cells were grown on the grids at 37°C for 20 hours to ensure that cells were in the fast-growing phase. Vitrification was performed using a manual plunger manufactured in the Max Planck Institute of Biochemistry, Martinsried, Germany. Grids with cells were quickly washed with PBS solution containing 10 nm protein A-conjugated gold beads (Aurion, Germany), blotted for 2 sec from the backside, and then plunged into a liquid ethane/propane mixture at liquid nitrogen temperature. Frozen grids were stored in a sealed box in liquid nitrogen until further use.

### 2.2. Microscopy: single images

Images were acquired on the SALVE microscope [6], and on a Titan Krios (Thermo Fischer Scientific, Eindhoven, The Netherlands). The SALVE microscope is a Titan Themis[3] microscope with a novel $C_c/C_s$ corrector based on the so-called Rose-Kuhn design incorporated [7]; it was equipped with a CETA 16M camera (Thermo Fischer Scientific). The Krios was equipped with a Quantum post-column energy filter and a K2 Summit direct detector camera (both from Gatan, Pleasanton, USA). The imaging conditions applied are summarized in Table 1.

With the SALVE microscope, selection of a particular defocus and correction of astigmatism was performed applying the so-called C1A1 tool, which uses the microscope's objective lens for focus adjustment and tunes the corrector's quadrupoles for astigmatism correction. We aimed at obtaining the zero crossings of the CTF at the same spatial frequencies at the different acceleration voltages. For that purpose, we derived the defocus at a particular acceleration voltage from that at the

acceleration voltage used before by keeping the defocus term of the wave aberration function constant ($\lambda Du^2$; see Section 2.5); the spherical aberration term is zero with the SALVE microscope. We also aimed at keeping the defocus relatively small in order to be well able to trace the Thon ring modulations up to high spatial frequencies. However, while we started at 80 kV, we observed that applying the C1A1 tool became more difficult with decreasing defocus and increasing object thickness, and realized that the situation would aggravate with decreasing acceleration voltages. Therefore, we started with using three defoci.

With the Krios, the defoci were selected at random. Yet, the positions of the zero crossing at 500 nm defocus happened to coincide with those at 250 nm at 80 kV, etc., with the SALVE microscope. Data was acquired using the SerialEM software [8,9]. The images were recorded in dose-fractionation mode (exposure time 2 sec, frame time 0.1 sec, 20 frames).

### 2.3. Processing of the single images

Defoci were determined using established CTF search programs: CTFFIND4 [10] in the case of the images of carbon, and Gctf [11] with those of *Mycoplasma pneumoniae*.

Images were processed using DigitalMicrograph (Gatan, Pleasanton, USA); a laboratory-written script for calculating rotational averages was added to the package. Integrations of $\sin^2\chi$ (see Section 2.5) were carried out using a laboratory-written module in Excel (Microsoft Corporation, Redmond, USA). Fits of the results of the integrations with the rotational averages of power spectra were performed on the basis of visual inspection.

### 2.4. Electron tomography

Data was acquired on a first-generation Titan (Ulm University) and on a Titan Krios (EMBL; described above). The Titan was equipped with a 2k MSC CCD camera (Gatan); a dedicated specimen holder was used for tomography (Model 2020, Fischione, Export, USA). The operating conditions for tomographic data acquisition are summarized in Table 2.

*M. pneumonia* tilt series were collected at the positions where the single images had been acquired, applying a dose-symmetric tilt scheme [12].

Tilt series were processed in IMOD using fiducial-marker (colloidal gold) or patch tracking (evaporated gold), and weighted back projection reconstruction [13]. Final alignment of the tilt-series images was performed using the linear interpolation option in IMOD without CTF correction. Cell thicknesses in vitrified specimens were estimated using central YZ sections of the tomograms. Carbon foil thicknesses were measured in ImageJ.

### 2.5. Model for describing the power spectra

The power spectra can be described following the approach taken earlier by De Rosier [1] and McMullan *et al.* [2], *i.e.* by integrating over the power spectra of successive, infinitesimally thin, independently scattering slices perpendicular to the beam. Following the latter authors' notation, the power spectrum $S(u)$ can be represented by:

$$S(u) \propto \langle |V_p(u)|^2 \rangle \int_{-t/2}^{+t/2} \sin^2\chi(u, D + z)\, dz \tag{1}$$

where $V_p(u)$ is proportional to the Fourier transform of the projected potential of the atoms in the sample, *i.e.* the scattering factor, $u$ is the spatial frequency, $t$ is the object thickness, $\chi$ the wave aberration function

$$\chi(u) = 2\pi \left( \frac{\lambda}{2} Du^2 - \frac{\lambda^3}{4} C_s u^4 \right) \tag{2}$$

in which D is the objective lens defocus and $C_s$ the constant of spherical aberration.

**Table 1**
Single-image recording conditions

| Specimen | Microsc. | Accel.voltage (kV) | Wave length (pm) | $C_s$ (mm) | Temp. | Defocus (nm) | Imaging mode | Pixel size (nm) | Dose (e/nm$^2$) |
|---|---|---|---|---|---|---|---|---|---|
| Carbon | SALVE | 40 | 6.02 | 0 | ambient | 174, 201, 243 | TEM-bright field | 0.043 | $2.2 \times 10^5$ |
| | | 60 | 4.87 | | | 215, 249, 300 | | 0.046 | |
| | | 80 | 4.18 | | | 250, 290, 350 | | 0.051 | |
| | Titan Krios | 300 | 1.97 | 2.7 | 80 K | 400, 500, 600 | EFTEM (20 eV) | 0.051 | |
| Vitrified *M. pneumonia* | Titan Krios | 300 | 1.97 | 2.7 | 80 K | 200-500 | EFTEM (20 eV) | 0.063 | $3.2 \times 10^3$ |

The number of slices needed with the integration in order to attain stable results was determined empirically; forty appeared to be sufficient.

In addition to numerical integration, the results can also be described analytically using the equation that McMullan *et al.* (2015) derived from Eq. (1), using $\sin^2(\chi) = 1/2(1 - \cos(2\chi))$:

$$S(u) \propto \langle |V_p(u)|^2 \rangle \frac{1}{2} [1 - \mathrm{sinc}(\xi)\cos(2\chi(u, D))] \qquad (3)$$

where

$$\mathrm{sinc}(\xi) = \sin(\xi)/\xi \qquad (4)$$

and

$$\xi = \pi\lambda u^2 t. \qquad (5)$$

In this way, the thickness-induced modulation of the Thon ring intensities can be described by a sinc function, which will be zero for $\sin(\xi) = n\pi$, with $n = 1, 2, \ldots$ Accordingly, when working with different numbers of layers $l$ of carbon ($l = 1, 2, 3$, and sometimes 4), the thickness $t$ of a single layer can be derived from the spatial frequency $u$ for a particular node using Eq. (5) in the following way:

$$t = \frac{n}{l\lambda u^2} \qquad (6)$$

in which $n$ represents the node number (first, second…).

McMullan *et al.* note that the $\sin(\xi)/\xi$ ringing arises from the fixed thickness and uniform ("top-hat") profile that is implicit in Eq. (1). As an alternative approach, they add a "cosine" profile to the integral and derive a further analytical description (Not dealt with in detail here; see McMullan *et al.* [2]).

## 3. Results

Fig. 1 shows the main kind of specimen used for studying the thickness-induced contrast transfer damping; Fig. 1a is a light microscopic image and Fig. 1b an electron microscopic (EM) image. The specimen consists of up to three layers of carbon on a 300 mesh grid. The optical density of a single layer was measured to be 0.2; in this way, its thickness was assumed to be 20 nm (see Materials and Methods). Fig. 1c depicts a vertical section through a tomogram of a sister specimen; in this case, the specimen was coated with gold on both sides. The transitions between one-, two- and three-layer areas can be observed. The unit layer thickness was measured to be 13.5-14.0 nm. Apart from gold grains, also 5 and 10 nm colloidal gold beads were used as fiducial markers. In addition to measurements on horizontally oriented layers, also vertically oriented ones were measured in tomograms of specimen areas where foils had flipped over.

Fig. 2 displays power spectra of images of triple layer areas of specimens like the ones represented in Fig. 1. The images were recorded at acceleration voltages of 40, 60, 80, and 300 kV (Figs. 2a to 2d, resp.). "Irregularities", denoted by vertical arrows, are observed in the Thon ring patterns. While the Thon ring intensities in a particular pattern first decrease with increasing spatial frequencies in a manner that is expected, they increase again later; moreover, the regular pattern of decreasing distances between the rings is often seen to be interrupted at an intensity minimum (*cf.* Fig. 3, insets). We name these irregularities

"nodes". They move outward, to higher spatial frequencies, with increasing acceleration voltage; still, the node can be well observed at 300 kV. The horizontal arrow in Fig. 2a points at the scattering intensity maximum that correspond to a maximum in the structure factor of amorphous carbon. This peak appears at 4.6 nm$^{-1}$ (0.22 nm), and corresponds to the second interatomic C-C distance in amorphous carbon. The peak associated with the first interatomic C-C distance at 7.1 nm$^{-1}$ (0.14 nm) apparently disappears in the noise.

Fig. 3 presents rotational averages of the power spectra shown in Fig. 2; the insets show examples of the (small) intensity drops often observed in nodes, interrupting the regular pattern of decreasing distances between Thon rings. Corresponding to the observation that the nodes move to lower spatial frequencies with decreasing acceleration voltages, it is seen that attenuation of the Thon ring amplitudes, when going to higher spatial frequencies, becomes stronger in the same order. In addition to the nodes that are readily seen in the power specta (Fig. 2), second nodes can also be observed at higher spatial frequencies in the rotational averages. Sometimes, even third nodes can be discerned (red and green curves). The rotational averages also show the broad peak at ~4.6 nm$^{-1}$. The Thon rings lie on top of this peak. When considering one particular acceleration voltage (power spectra and rotational averages not shown), the nodes move to lower spatial frequencies with increasing thickness. At 80 kV, for example, the first nodes for one, two, and three layers of carbon are, on average, at $4.2 \pm 0.18$ nm$^{-1}$ (17 observations), $2.9 \pm 0.07$ nm$^{-1}$ (34), and $2.5 \pm 0.07$ nm$^{-1}$ (36), resp.

Fig. 4 depicts the statistical distribution for the unit carbon layer thickness, derived from the positions of the nodes, using Eq. (6). The positions were determined by visual inspection of plots of the rotational averages of the power spectra, as indicated by the arrows in Fig. 3. First, second and third nodes found with one, two, three and occasional four layers at 40, 60, 80, and 300 kV were included in the analysis (at 300 kV, only images of three and four layers were taken). The average single layer thickness was found to be $13.7 \pm 0.91$ nm; the number of observations was 386. Broken down by node number, these data are: first node– $13.8 \pm 0.97$ nm, 231 observations; second node– $13.6 \pm 0.83$ nm, 135; third node– $14.3 \pm 0.48$ nm, 16. Results that were clearly affected by hydrocarbon-caused contamination, were discarded (18% of the data; microscopy with the SALVE machine was at room temperature).

Fig. 5 introduces a real-world specimen that we used for validating our approach: frozen-hydrated *Mycoplasma pneumoniae* cells. First, a single image was taken at the center of a particular cell (Fig. 5a); the rotational average of this image's power spectrum was used for tracing possible nodes (Fig. 6b). Subsequently, a tilt series was recorded of the same cell at a larger pixel size. The XY-section of the reconstructed tomogram in Fig. 5b shows the cell membrane as well as ribosomes; Fig. 5a corresponds to the central area of Fig. 5b. The thickness of a particular cell was measured in XZ-cross-sections of a tomogram: 163 nm, in this case (Fig. 5c, vertical bar). In total, twenty-eight cells on the same grid were included in our analysis. Fig. 5d shows their thickness range: from 90 to 270 nm; the arrow denotes the cell studied in Fig. 5 and Fig. 6b.

Fig. 6 presents comparisons between rotational averages of power spectra and results of integrations of $\sin^2\chi$ over objects thicknesses at 300 kV (*cf.* Eq. (1); magenta-colored curves), that best fitted the

**Table 2**
Tomogram recording conditions

| Specimen | Microsc. | Temp. | Imaging mode | Tilt from (degr.) | to (degr.) | step (degr.) | Tilt control | Tilt-angle distribution | Pixel size (nm) | Dose / tilt (e/nm$^2$) |
|---|---|---|---|---|---|---|---|---|---|---|
| Carbon | Titan | amb. | TEM-bright field | -60 | +60 | 1 | manual | linear | 1.0 | $7.5 \times 10^3$ |
|  | Titan Krios | 80 K | EFTEM (20 eV) | +65 | -65 | 0.5 | SerialEM | lin., cosine | 0.21 | $5 \times 10^2$ |
| Vitrified *M. pneumonia* | Titan Krios | 80 K | EFTEM (20 eV) | -60 | +60 | 3 | SerialEM | linear | 0.17 | $3.1 \times 10^2$ |

Acceleration voltage: 300 kV

rotational averages. For the numerical calculations, the object is thought to lie half below, half above the selected objective lens defocus. The results of the integrations oscillate around 0.5, the initial minimum and maximum values being 0 and 1, resp. (secondary Y-axis of Fig. 6b).

In Fig. 6a, the object is a triple carbon layer foil (cyan, as in Fig. 3b). The fit is on the basis of a thickness of 40.8 nm (13.6 nm for a single layer), and an objective lens defocus of 507 nm. It was attained on the basis of visual inspection, starting from the values that were known beforehand and varying the parameter values in an iterative manner. The match extends out to a spatial frequency of ~6 nm$^{-1}$ (0.16 nm). It is from the fit over this resolution range that the value for the defocus is derived. By contrast, the value for the thickness is only determined from a fit with the positions and the features seen for the nodes in the rotational average. The irregularity observed above 6.2 nm$^{-1}$ in the fit arises from the $C_s$ term in the wave aberration function (Eq. (2)). With the images recorded with the SALVE microscope, the constant for spherical aberration was taken to be zero when fitting the rotational averages. Fitting the same data with CTFFIND4 [10], a defocus of 501 nm was found. The spatial frequency at which the cross-correlation (CC) between the CTF and the pattern crosses zero was 3.49 nm$^{-1}$. This value is close to that found for the position of the first node, 3.54 nm$^{-1}$, established by visual inspection of the rotational average (*cf*. Fig. 3). This value, in turn, corresponds to a thickness of 40.5 nm (13.5 for a single layer).

This fitting analysis was extended over 38 more images of three and also four layers of carbon. On average, the defocus used for the fits was 101.0 ± 0.43 % of that found with CTFFIND4. The spatial frequency for the first node detected by direct visual inspection was 99.2 ± 1.42 % of that for the CTFFIND4 CC zero crossing. The unit carbon layer thickness derived by fitting was 13.6 ± 0.23 nm, compared with 13.7 ± 0.34 in the case of direct visual detection of the nodes (75 observations; one rotational average could not be interpreted with respect to the object's thickness).

In Fig. 6b, the object is a frozen-hydrated *Mycoplasma pneumoniae* cell shown in Fig. 5a (green trace). First and second nodes can be readily recognized when visually inspecting the rotational average (arrows). They lie at ~1.70 and ~2.37 nm$^{-1}$, resp., corresponding to a thickness of ~178 nm (*cf*. Eq. (6)). The result of the $\sin^2\chi$ integration has been obtained with an object thickness $t = 172$ nm, a defocus $D = 653$ nm (691 nm had been found with Gctf [11]), and a constant of spherical aberration $C_s = 2.70$; the match extends out to ~3.2 nm$^{-1}$ (0.31 nm). A value of 172 nm derived for the thickness in this way, is ~1.1x the value estimated with tomography (*cf*. arrow in Fig. 5d). The structure factor of the specimen represents a combination of the scattering from the bacterium and the vitrified water; a peak is appearing at 2.7 nm$^{-1}$ (0.37 nm).

The same approach was applied to 27 more bacterial cells on the same grid with tomographically determined thicknesses varying from 90 to 270 nm (Fig. 5d). Direct visual localization of the nodes was possible up to a thickness of 175 nm; with thicker specimens, the Thon ring's amplitudes became too small to recognize irregularities in the patterns. The localization of the nodes was easier at relatively high defocus, as used in the case of Fig. 6b. All radial density profiles could be fitted by numerical integration, except one: in that case, the defocus as determined with Gctf was only 203 nm, yielding too featureless a Thon ring pattern. On average, the specimen thickness derived via this analysis was 1.1x higher than the one estimated by tomography, independent from the approach followed - visual node localization or fitting by numerical integration. The defocus found was 96 ± 9 % of that measured with Gctf, and the match extended out to almost 3 nm$^{-1}$. One outlier with a tomographically measured thickness of 90 nm was discarded.

## 4. Discussion

We have shown experimentally, what a Thon ring pattern can look
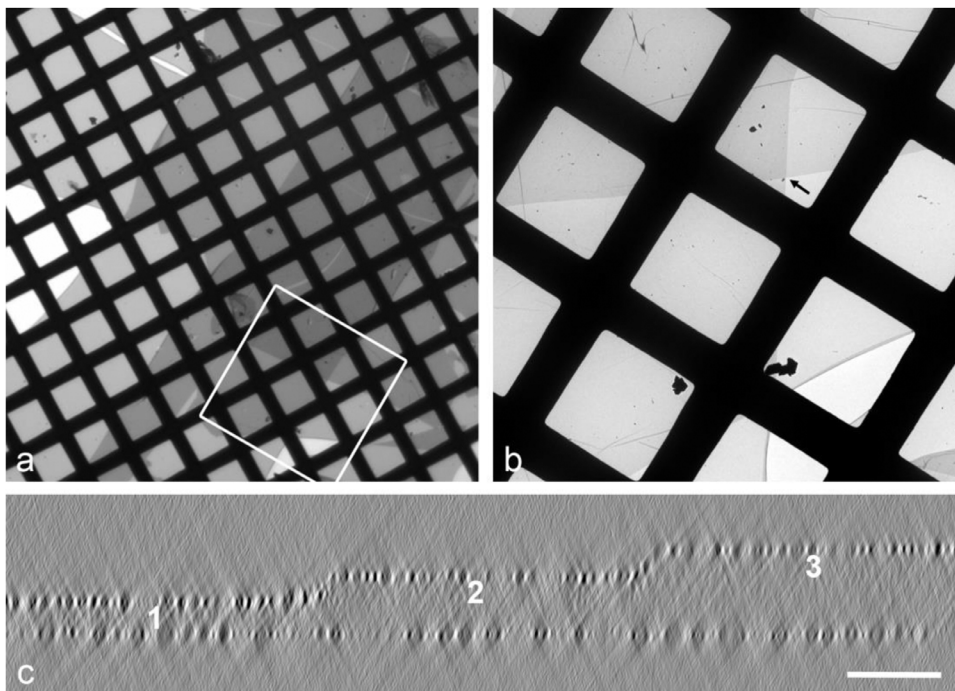
**Fig. 1.** Carbon foil specimen used to study the thickness-induced attenuation of contrast transfer. (a) Overview light-microscopic picture showing strips of carbon film layered on top of one another on a 300 mesh grid (1 square + 1 bar = 84.7 μm). The frame indicates the area displayed in (b), which is an EM image. The arrow points at a region where single, double and triple layer areas are adjacent to one another. (c) Vertical cross-section through a tomogram of a region similar to the one specified by the arrow in (b). The numbers indicate the areas with one, two and three layers of carbon, resp. This specimen was coated with gold grains on both sides. Bar = 50 nm.

like when a specimen becomes too thick for the Ewald sphere to be considered flat or, expressed differently, when the object becomes too thick to be represented by a single defocus. In this respect, we were aided, originally, by applying relatively low acceleration voltages (40, 60, and 80 kV), while using an electron microscope with a high resolving power. Linck *et al.* [6] found the information limit for the SALVE microscope at 40, 60, and 80 kV to be at 90, 83, and 76 pm, resp. With an uncorrected microscope, the information limit would hardly be sufficient to identify thickness-induced damping at these acceleration voltages. Furthermore, the use of a test object that could endure a relatively high electron dose, *i.e.* carbon film, was also helpful.

In addition, we were able to experimentally confirm, that the Thon ring pattern of a thick object can be considered to be the sum of patterns originating from independently scattering slices; the determination of the object thickness, by tomography, was essential in this respect. Thus, a Thon ring pattern can be described by numerically integrating $\sin^2\chi$ ($\chi$ is the wave aberration function; Eq. (2)) over the thickness of the object, lying half above, half below the selected objective lens defocus. The result is a modulation of the Thon ring amplitudes by a sinc function (Eq. (4)), *i.e.* the Fourier transform of a top hat profile.

Since we determined the object thickness and because we could detect higher nodes, we were also able to discriminate between the

analytical expressions already proposed by others for describing the Thon ring patterns. The "top-hat" expression by McMullan *et al.* [2] yields a profile that agrees with our experimental results. However, their "cosine" approximation, as well as the expression derived by DeRosier [1], do not. When comparing the "cosine" pattern with the "top-hat" one for a particular thickness, McMullan *et al.* already observed that the nodes move up one position. Conversely, this difference implies that, when a "cosine" pattern is fitted to experimental data, the position of the first node will correspond to an object that is two times too thick, while the positions of the higher nodes cannot be interpreted.

Furthermore, we demonstrated that our approach can be applied to thick biological cryo-specimens (up to ~270 nm in our case) under conditions commonly used for biological objects (a dose of $3.2 \times 10^3$ e/ nm$^2$, and an acceleration voltage of 300 kV). The fits, on the basis of visual inspection, between results of the integration of $\sin^2\chi$ and rotational averages of power spectra yield thicknesses that differ only marginally from those obtained with tomography; the deviation is possibly due to the fact that the tomographic series were acquired after the single images, and mass loss may have occurred along the way. The differences between the defoci found and those derived with Gcft [11] can be explained by possible flaws on both sides: misjudgment of a fit on our side and inaptness of a CTF fitting program such as Gcft to deal with irregularities in a Thon ring pattern (see also below).
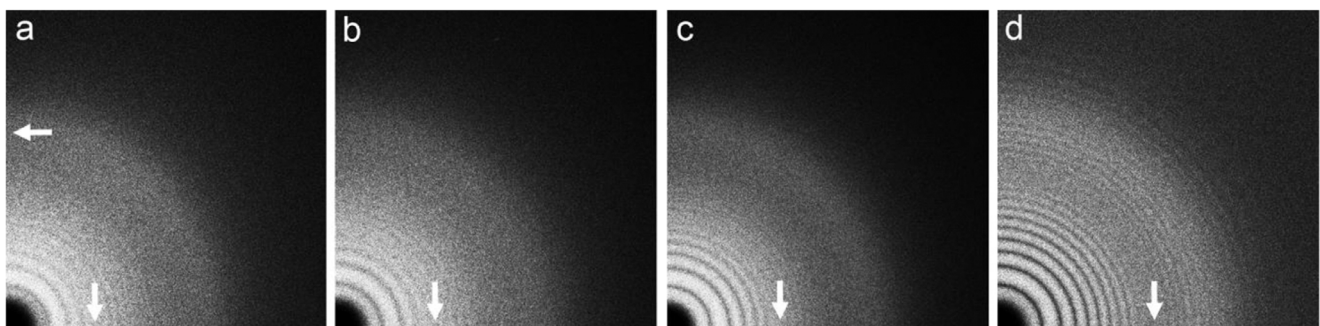


**Fig. 2.** Series of power spectra of images of triple layers of carbon (*cf.* Fig. 1), recorded at 40 kV (a), 60 kV (b), 80 kV (c) and 300 kV (d), showing "irregularities" in the Thon ring pattern (vertical arrows) which move to higher spatial frequencies with increasing acceleration voltage. The horizontal arrow points at the peak arising from near order in carbon at 0.22 nm. The patterns as displayed go out to 7.3 nm$^{-1}$ (~0.75 Nyquist).
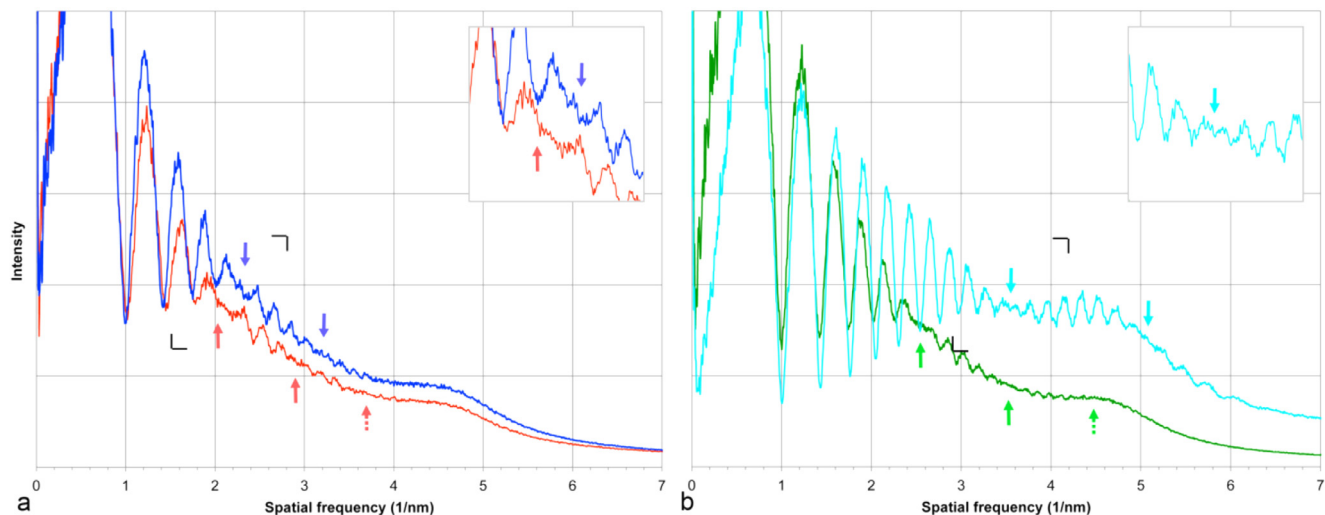
**Fig. 3.** Rotational averages of the power spectra in Fig. 2: the red and blue curves in (a) represent 40 kV and 60 kV, and the green and cyan ones in (b) correspond to 80 and 300 kV, resp. Colored arrows point at the first and second "nodes", occurring at the respective acceleration voltages; in the red and green traces, also third nodes can be discerned (dashed arrows). Brackets delineate areas containing first nodes, enlarged in insets.
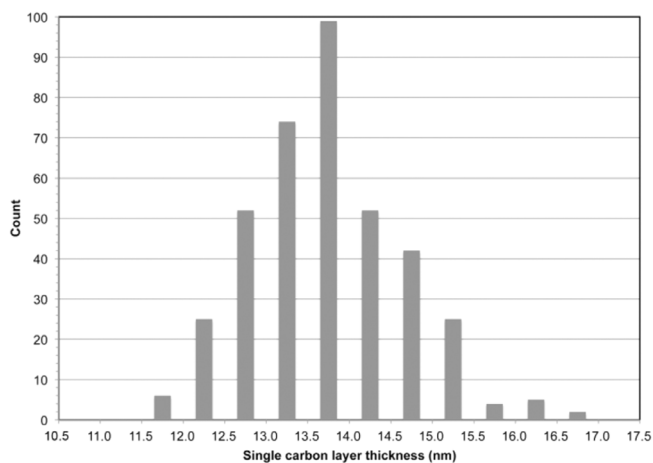


**Fig. 4.** Distribution for the unit carbon layer thickness derived from positions of first, second and third nodes for single, double and triple carbon layers at 40, 60, 80, and 300 kV. The average is 13.7 nm, the standard deviation 0.91 nm, and the number of observations 386.

Whereas the defocus is determined from a fit with the pattern over the entire range that contains information, the thickness is derived from a match with the positions and features of the nodes. We performed these fits without subtraction of the background, which is sloping, and noticed that the thickness values derived from fitting tended to be somewhat smaller than those determined by direct localization of the nodes in the patterns. Therefore, we anticipate that future fitting by computer programs will benefit from background subtraction.

For the sake of completeness, it is probably useful to point out, that integrating $\sin \chi$ over the thickness of the object, and then squaring the result, will not give correct node positions: while $\text{sinc}(\pi \lambda u^2 t)$ is the sinc function resulting from the integration of the power spectra (Eqs. (3) to (5)), it will be $\text{sinc}(\pi \lambda u^2 t/2)$ when integrating the transfer functions; squaring a sinc function will leave the positions of nodes unaffected. With $\text{sinc}(\pi \lambda u^2 t/2)$, the node positions, when fitted to experimental data, will give values for the object thickness that are two times too high.

A prerequisite for accurate 3D reconstruction is correct knowledge about the defocus of each image element involved, in order to be able to apply the appropriate correction for the CTF up to the resolution aimed at. This defocus is usually determined by fitting the absolute value or

the square of the CTF to a Thon ring pattern. While $\sin \chi$ is the CTF in the case of thin objects, it will be $\text{sinc}(\xi) \cdot \sin \chi$ in the case of thicker ones (*cf.* Eqs. (4) and (5)); thus, the sign for the CTF will be reversed after each node (Fig. 7a). In both cases however, fitting to the Thon ring pattern will only be successful up until the first node and between the second and the third node where a maximum value for a Thon ring amplitude will, as usual, correspond to a maximum of the absolute value or the square of the CTF (Fig. 7b); contrary, a maximum is seen to coincide with a minimum in the Thon ring pattern, and *vice versa*, between the first and the second node, etc. While occurring with thick objects in general, the situation will become even more pronounced in the case of tomography: the apparent object thickness will additionally increase with increasing tilt angle. We have shown, that a match over the full resolution range that contains signal will be attained by integrating $\sin^2 \chi$ over the thickness of the object. In this way, not only the correct value for the defocus is obtained, but also the object thickness is determined. Still, correction for the CTF as usual can probably not be applied over the full resolution range in the case of a real-life, inhomogeneous object using the function $\text{sinc}(\xi) \cdot \sin \chi$: its postulation is based on the assumption that the object can be considered to consist of slices that scatter independently.

When analyzing large single particles, the approach to appropriate CTF correction that has been taken until now is to separately determine the amplitudes and phases of the Fourier components that would be Friedel-related for a thin object. This determination can be achieved in several ways, one being the application of a larger defocus which physically separates the Fourier fringes in the image, allowing to use two single sideband CTFs [14,15]. Russo & Henderson [15] additionally apply a masking step that removes any contribution from the incorrect, pseudo-Friedel-related Fourier component (Their method is implemented in RELION [16]). The authors point out that the defocus necessary to record the two pseudo-Friedel-related Fourier components separately in the image is $tu/2\lambda$ (meaning of symbols as in Section 2.5). We have shown here, that the relevant value of $t$ can be deduced from the position of the nodes, determined by direct visual inspection (Figs. 3 and 4) or by fitting with the integral of $\sin^2 \chi$ (Fig. 6).

This approach applies to the situation in which a large object determines the thickness of specimen, and tomography is not applied. When a smaller object is located at different heights in a thicker specimen, other methods are available that allow the defocus applied with CTF correction for a particular set of voxels to be established correctly: for example, by using a 3D reference structure with single particle analysis [16], and by 3D-CTF correction in the case of tomography
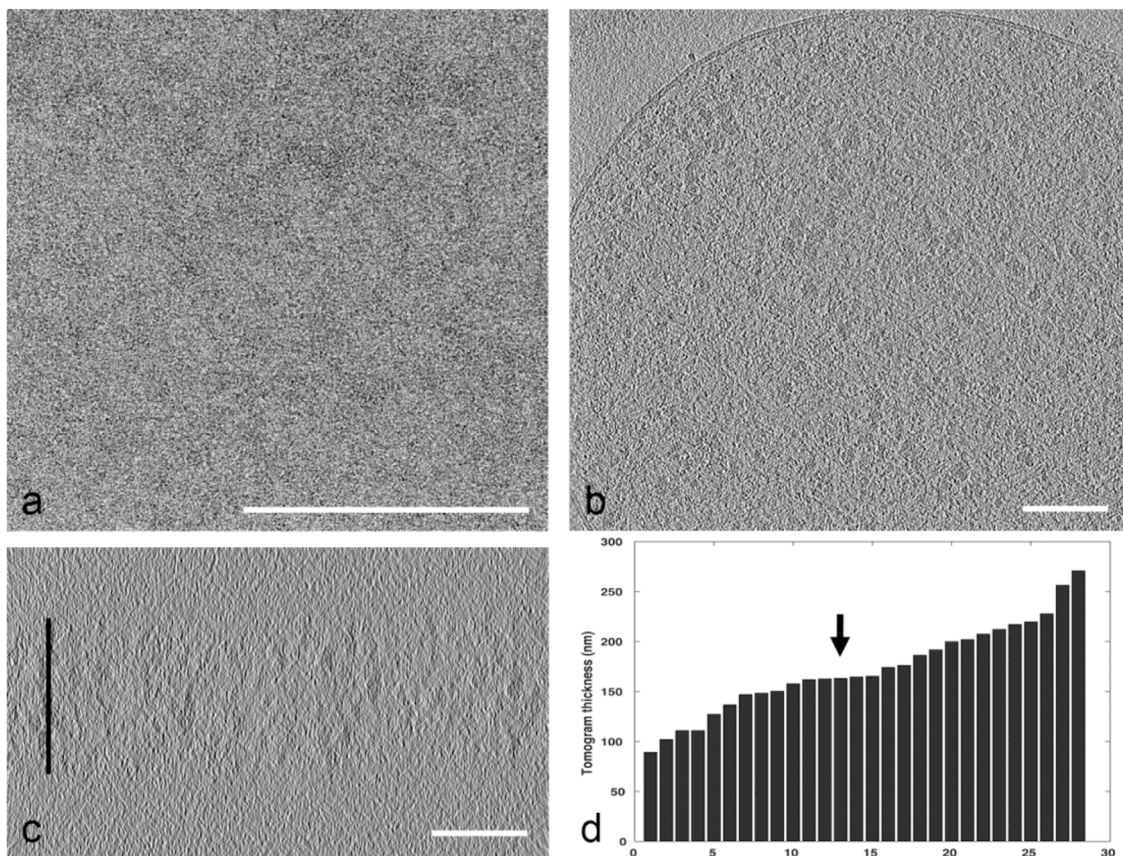
**Fig. 5.** Example of a frozen-hydrated *Mycoplasma pneumoniae* cell used for validation of our approach: (a) single 2D image; (b) XY section of a reconstructed tomogram (Fig. (a) corresponds to the central area of Fig. (b)); (c) XZ-cross-section of a reconstructed tomogram allowing to measure the cell thickness (vertical bar), and (d) graph displaying the thicknesses of the 28 cells studied. Arrow denotes the cell analyzed in this Figure, and in Fig. 6b. Bars = 100 nm.

[17].

The implications of our study complement the perspective on TEM of biomacromolecules as it is currently outlined by Henderson and colleagues (*e.g.* Peet *et al.* [3]; Naydenova *et al.* [4]): that it is worth considering moving back to acceleration voltages lower than the 300 kV commonly applied now; with decreasing energy, the amount of

information that becomes available increases more strongly than the damage that occurs; the optimum energy would be 100 keV. Should the field move into this direction, then properly dealing with thickness-induced attenuation of the contrast transfer will become more important. The spatial frequencies at which the first nodes occur as a function of specimen thickness ($u = \sqrt{1/\lambda t}$) at 300 and 100 kV, resp.,
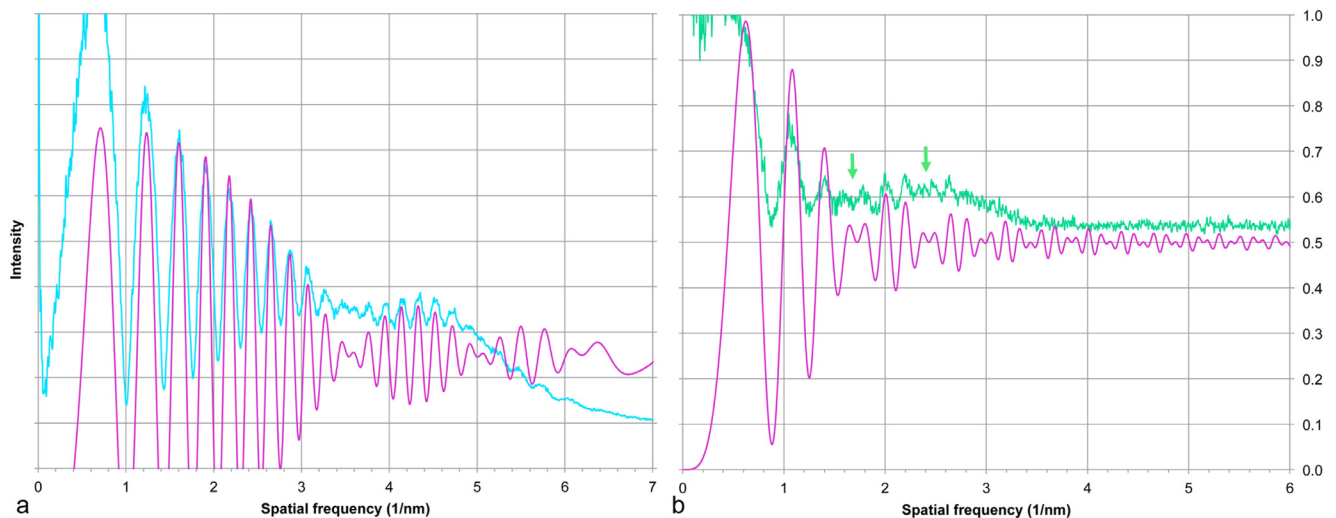


**Fig. 6.** Comparisons of rotational averages of power spectra (primary Y-axes) with results of integrations of $\sin^2\chi$ (*cf.* Eq. (1)) over the thickness of an object at 300 kV (magenta; secondary Y-axes): (a) for a triple layer of carbon (cyan, as in Fig. 3b), applying a thickness $t$= 40 nm, an objective lens defocus $D$= 507 nm, and a constant of spherical aberration $C_s$= 2.76 mm (shifted downward in order to better illustrate the fit); (b) for a frozen-hydrated *Mycoplasma pneumonia* bacterium (green; Nyquist = 7.9 nm$^{-1}$), using $t$= 172 nm, $D$= 653 nm, $C_s$= 2.70.
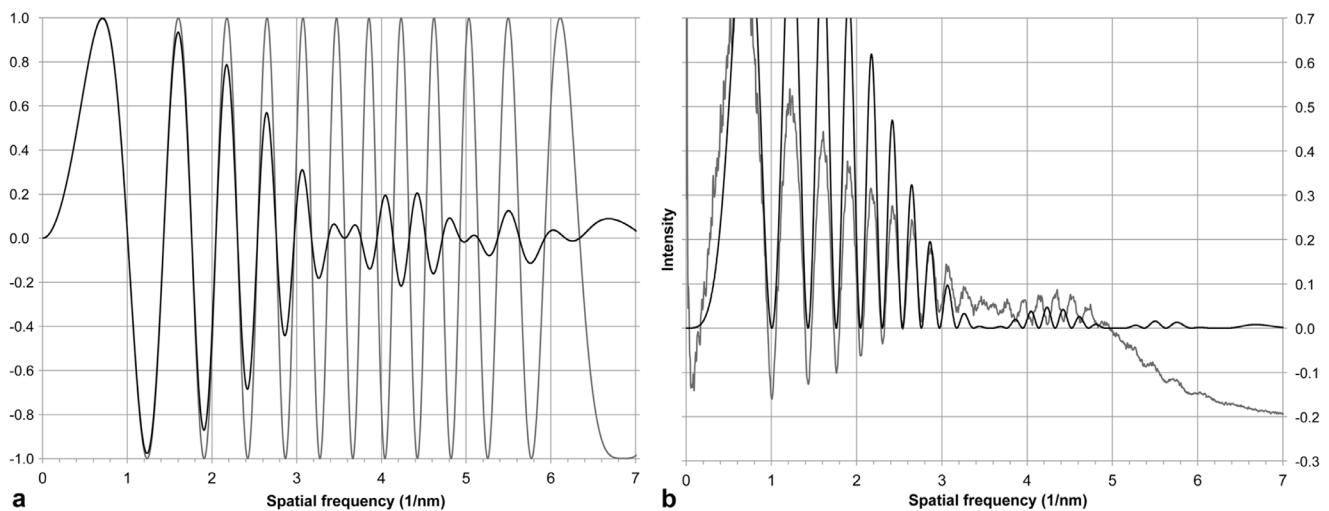
**Fig. 7.** (a) Comparison of a plot of $\mathrm{sinc}(\xi) \cdot \sin \chi$ (black; see Text) with one of the conventional CTF, $\sin \chi$ (grey). (b) Fit of the square of the CTF, *i.e.* $(\mathrm{sinc}(\xi) \cdot \sin \chi)^2$ (black, shifted upward, secondary Y-axis), with the rotational average of a power spectrum (grey, primary Y-axis). The conditions are as in Fig. 5a.
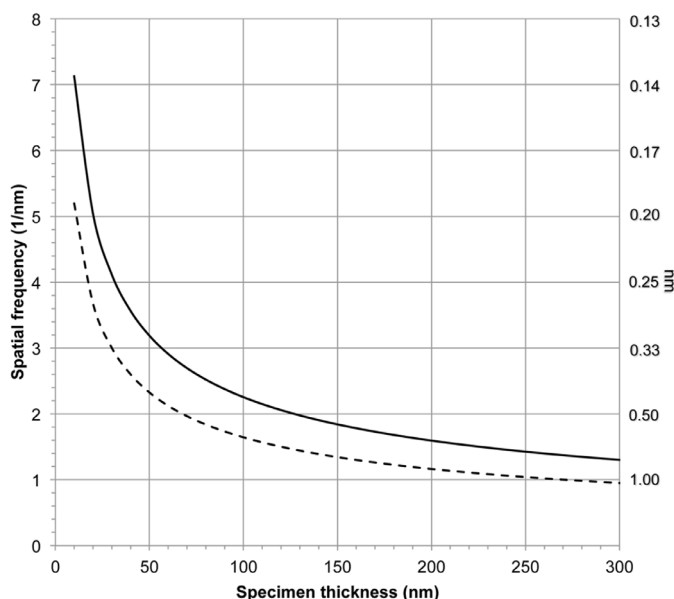


**Fig. 8.** Plots of the spatial frequency for the first node as a function of the object thickness ($u = \sqrt{1/\lambda t}$) at 100 and 300 kV (dashed and solid lines, resp.)

are compared in Fig. 8. With a specimen thickness of 75 nm, for example, the first node will shift from 2.6 nm$^{-1}$ (0.38 nm) to 1.9 nm$^{-1}$ (0.53 nm), when going from 300 kV to 100 kV. Furthermore, Naydenova *et al.* note that a small chromatic aberration coefficient ($C_c$) is more important at 100 kV than at 300 kV. With the SALVE machine at 80 kV, we acquired images also without $C_c$-correction; that is, $C_c$ was 1.45 mm, instead of 15 µm. Under those conditions, we could detect the second nodes only for the triple layers of carbon (at ~3.5 nm$^{-1}$ (0.29 nm)), whereas we could observe those nodes already for the double layers, when $C_c$ was corrected (at ~4.4 nm$^{-1}$ (0.23 nm)).

With Fig. 3, we noted that the attenuation of the Thon rings with rising spatial frequencies increases with decreasing acceleration voltage and increasing thickness; we put this attenuation in relation to the nodes moving to lower spatial frequencies. However, it can also be seen in Fig. 3, that the amplitudes of the Thon rings decrease, in the order mentioned, from the onset, *i.e.* starting at low spatial frequencies. Multiple, elastic and inelastic scattering will also cause this effect. An investigation of the relative contribution by this mechanism however, has not been part of this study.

## 5. Conclusions

Determination of the accurate defocus to be applied with CTF correction in the case of an object whose thickness exceeds the microscope's field of view, can be achieved by fitting the Thon ring pattern with the result of a numerical integration of power spectra originating from thin, independently scattering slices over the object thickness. In this way, a match is attained over the full resolution range that contains signal. The positions of the nodes observed in the pattern, determined via fitting or by direct visual inspection of rotational averages, will yield the value for the object thickness. Classical fitting of just the CTF to a power spectrum will only be successful up until the first node, and between the second and third nodes.

## Declaration of Competing Interest

None.

## Acknowledgments

## Supplementary materials

Supplementary material associated with this article can be found, in the online version, at doi:10.1016/j.ultramic.2020.113023.

# References

[1] D.J. DeRosier, Correction of high-resolution data for curvature of the Ewald sphere, Ultramicroscopy 81 (2000) 83–98, https://doi.org/10.1016/S0304-3991(99)00120-5.

[2] G. McMullan, K.R. Vinothkumar, R. Henderson, Thon rings from amorphous ice and implications of beam-induced Brownian motion in single particle electron cryo-microscopy, Ultramicroscopy 158 (2015) 26–32, https://doi.org/10.1016/j.ultramic.2015.05.017.

[3] M.J. Peet, R. Henderson, C.J. Russo, The energy dependence of contrast and damage in electron cryomicroscopy of biological molecules, Ultramicroscopy 203 (2019) 125–131, https://doi.org/10.1016/j.ultramic.2019.02.007.

[4] C. Cb, K. Naydenova, G. Mcmullan, M.J. Peet, Y. Lee, P.C. Edwards, S. Chen, E. Leahy, S. Scotcher, R. Henderson, C.J. Russo, CryoEM at 100 keV: a demonstration and prospects, (2019) 1–31. 10.1107/S2052252519012612.

[5] A.W. Agar, The measurement of the thickness of thin carbon films, Br. J. Appl. Phys. 8 (1957) 35–36, https://doi.org/10.1088/0508-3443/8/1/310.

[6] M. Linck, P. Hartel, S. Uhlemann, F. Kahl, H. Müller, J. Zach, M. Haider, M. Niestadt, M. Bischoff, J. Biskupek, Z. Lee, T. Lehnert, F. Börrnert, H. Rose, U. Kaiser, Chromatic Aberration Correction for Atomic Resolution TEM Imaging from 20 to 80 kV, Phys. Rev. Lett. 117 (2016) 1–5, https://doi.org/10.1103/PhysRevLett.117.076101.

[7] H. Rose, Correction of aberrations - a promising method for improving the performance of electron microscopes., in: Proc. 10th Eur. Congr. Electron Microsc. Granada, Spain, Secretariado de Publicaciones de la Universidad de Granade, Granada, 1992.

[8] D.N. Mastronarde, Automated electron microscope tomography using robust prediction of specimen movements, J, Struct. Biol. 152 (2005) 36–51, https://doi.org/10.1016/j.jsb.2005.07.007.

[9] M. Schorb, I. Haberbosch, W.J.H. Hagen, Y. Schwab, D.N. Mastronarde, Software tools for automated transmission electron microscopy, Nat. Methods. 16 (2019) 471–477, https://doi.org/10.1038/s41592-019-0396-9.

[10] A. Rohou, N. Grigorieff, CTFFIND4: Fast and accurate defocus estimation from electron micrographs, J. Struct. Biol. 192 (2015) 216–221, https://doi.org/10.1016/j.jsb.2015.08.008.

[11] K. Zhang, Gctf: Real-time CTF determination and correction, J. Struct. Biol. 193 (2016) 1–12, https://doi.org/10.1016/j.jsb.2015.11.003.

[12] W.J.H. Hagen, W. Wan, J.A.G. Briggs, Implementation of a cryo-electron tomography tilt-scheme optimized for high resolution subtomogram averaging, J, Struct. Biol. 197 (2017) 191–198, https://doi.org/10.1016/j.jsb.2016.06.007.

[13] D.N. Mastronarde, S.R. Held, Automated tilt series alignment and tomographic reconstruction in IMOD, J, Struct. Biol. 197 (2017) 102–113, https://doi.org/10.1016/j.jsb.2016.07.011.

[14] M. Wolf, D.J. DeRosier, N. Grigorieff, Ewald sphere correction for single-particle electron microscopy, Ultramicroscopy 106 (2006) 376–382, https://doi.org/10.1016/j.ultramic.2005.11.001.

[15] C.J. Russo, R. Henderson, Ewald sphere correction using a single side-band image processing algorithm, Ultramicroscopy 187 (2018) 26–33, https://doi.org/10.1016/j.ultramic.2017.11.001.

[16] J. Zivanov, T. Nakane, B.O. Forsberg, D. Kimanius, W.J.H. Hagen, E. Lindahl, S.H.W. Scheres, New tools for automated high-resolution cryo-EM structure determination in RELION-3, Elife 7 (2018) 1–22, https://doi.org/10.7554/eLife.42166.

[17] B. Turoňová, F.K.M. Schur, W. Wan, J.A.G. Briggs, Efficient 3D-CTF correction for cryo-electron tomography using NovaCTF improves subtomogram averaging resolution to 3.4 Å, J, Struct. Biol. 199 (2017) 187–195, https://doi.org/10.1016/j.jsb.2017.07.007.